



# Least-squares local Radon transforms for dip-dependent GPR image decomposition

Ulrich Theune <sup>\*</sup>, Mauricio D. Sacchi, Douglas R. Schmitt

*Geophysical Institute, Department of Physics, University of Alberta, Edmonton, Alberta, T6G 2J1, Canada*

Received 15 July 2005; accepted 10 October 2005

## Abstract

GPR is a powerful tool for geophysical near-surface investigations. It is capable of delivering a high-resolution image of the subsurface structure. However, if the underground consists of many reflecting events, the analysis and interpretation of the data can be very complicated. In this paper, we present a new image decomposition technique that is based on Local Radon transforms. This technique is a parametric local dip-decomposition method that allows us to extract features from or reconstruct GPR data.

In addition, it can also be applied to determine coherence attributes from the data. In particular, we show that after reconstructing the data with only a subset of dips, the interpretability of GPR images improves significantly in as such that reflectors in the migrated images are much easier to detect. We demonstrate the capabilities of this technique at GPR data acquired at the highly fractured summit of Turtle Mountain (Alberta/Canada).

© 2005 Elsevier B.V. All rights reserved.

**Keywords:** Ground penetrating radar; Dip filtering; Image decomposition; Local Radon transforms; Data coherence analysis

## 1. Introduction

Ground penetrating radar (GPR) has become a frequently employed technique in geo-physical near surface investigation. The electromagnetic waves employed in GPR studies are sensitive to the dielectric properties of the subsurface material. Hence, GPR data are processed to obtain an image of the dielectric structure of the subsurface with high vertical and horizontal resolution. It has therefore gained popularity for near-surface studies in many civil engineering and environmental applications (e.g., Zeng and McMechan, 1997) as well as archaeological studies (e.g., Goodman et al., 1995), among others.

When interpreting seismic or GPR data, we usually look for events that are coherent in some sense over a certain portion of the data set. For example, such coherent events could be diffraction hyperbolas indicating a strong scattering anomaly in the subsurface or continuous events that are related to a geological structure. However, especially with highly resolving techniques such as GPR, such coherent features may be hidden when numerous reflectors overlap. Then, the underlying structure is difficult to detect, which hampers the interpretation and risks the success of the survey. An example for this problem is the GPR data that were acquired at Turtle Mountain, Canada, to map bedding planes and fractures for a slope stability estimation project (Theune et al., in press). Fig. 1 displays a GPR data set acquired with a 50 MHz antennae system. The data set consists of 465 traces with 837 data points along each trace. We

\* Corresponding author. Fax: +1 780 492 0714.

E-mail address: [utheune@phys.ualberta.ca](mailto:utheune@phys.ualberta.ca) (U. Theune).

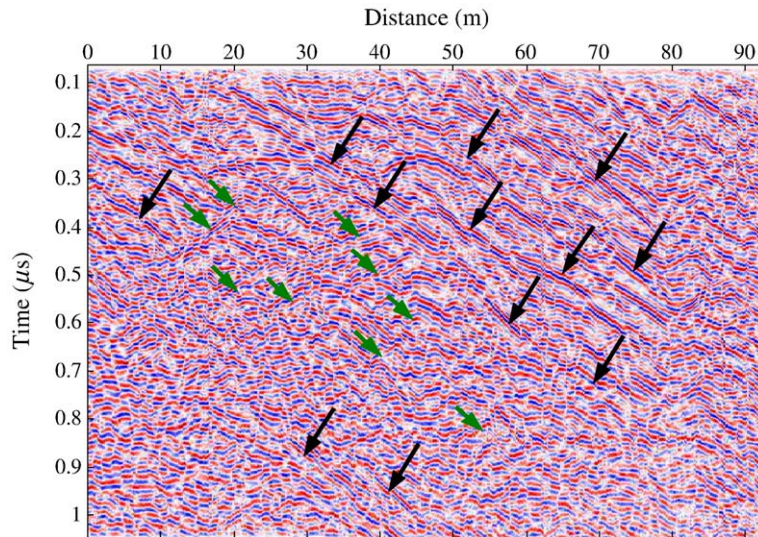


Fig. 1. GPR data acquired at Turtle Mountain. Black arrows indicate the “downward dipping” pattern of reflectors, green arrows point to “upward dipping” reflectors.

have applied only automated gain control to the data to amplify amplitudes for later arrival times and simple trace shifting to correct for small scale topographic variations.

The highly fractured nature of Turtle Mountain’s summit becomes apparent in numerous reflectors that differ in length and dip in the data. Despite the pattern of almost randomly distributed short scale events, there seem to be two reflector systems that appear to be more coherent over the data set. These two systems are indicated by black and green arrows in Fig. 1. However, the presence of small scale reflections complicates the detection of these events and the interpretation of the data significantly. Therefore, a processing algorithm to enhance or extract the interesting events in the data would improve the interpretation of the GPR data substantially.

Several techniques have been developed to extract coherent features in geophysical data. Generally, a method that allows the transformation of the data to a domain where the overlapping dips are separated is desirable. For further processing and analysis of the data, we must also require that the transform is invertible. In other words, two canonical transformations are needed, one to map the data to a new domain (inverse transform), the second to map the data from the transform domain back to the original domain (forward transform).

A common tool in seismic data processing to improve feature interpretation is based on coherence analysis (e.g., Foster and Guinzy, 1967; Mack, 1974; Marfurt et al., 1998; Cohen and Coifman, 2002).

These algorithms search for disruption in data continuity that may be related to faults, channel structures, and salt domes. However, coherency techniques fail if the data to be analyzed are too noisy or composed, like in our study, of a large superposition of events of different characteristic length and dip. Additionally, these algorithms transform the data to a domain where coherency anomalies are highlighted, and do not allow for an inverse transformation to reconstruct the data. In other words, coherence methods that are designed for data analysis and feature extraction do not produce a transform pair capable of analyzing and reconstructing the data.

Dip-dependent image decomposition can also be achieved by applying 2-D Fourier transforms to the data. The popular  $f-k$  (frequency-wavenumber) filtering techniques are frequently used in seismic processing to separate signals propagating with different velocities such as surface waves and reflected wave energy (e.g., Yilmaz, 1987). Such events also distinguish themselves through different dips in the  $t-x$  domain. Hence, the  $f-k$  filtering technique should also be applicable for the image decomposition of the GPR data set. However, the success of  $f-k$  filtering depends strongly on the degree to which events with different dips are mapped into distinguished regions in the  $f-k$  domain. If, for example, many events with similar dips are present in the data, these events overlap in the  $f-k$  domain and their separation is complicated.

To circumvent this inherent problem of  $f-k$  filtering for coherent noise suppression, Nuzzo and Quarta (2004) employed linear Radon and wavelet transforms.

Radon transforms have a long history in seismic data processing to separate coherent noise from signal (e.g., Hampson, 1986). Radon transforms can be interpreted as a summation of data amplitudes along predefined trajectories. Most common in geophysical applications are simple trajectories such as linear, parabolic, and hyperbolic summation paths (e.g., Trad et al., 2003). These trajectories are characterized by two parameters: the intercept time  $\tau$  and, in the case of the linear Radon transform, the dip (or slowness)  $p$ , and the velocity  $v$  in the parabolic and hyperbolic case, respectively. If, for example, a linear coherent event is aligned along a linear trajectory, the summation will result in a large value in the Radon domain for that particular  $\tau-p$  value pair. This event will then be distinguishable from other linear coherent events by its location in the Radon domain. By using linear Radon or  $\tau-p$  transforms, Nuzzo and Quarta (2004) were able to improve the coherent noise suppression in GPR data. In principle, Radon transforms can also be applied to dip-dependent image decomposition. However, full-aperture transforms, as they are usually applied in seismic processing and by Nuzzo and Quarta (2004), do not honor the local character of dip variations. Hence, a localized approach to the application of Radon transforms would serve the image decomposition better in such that the transform can be adapted to dip variability.

In this paper, we describe a method that employs the concepts of generalized convolution/deconvolution and local linear Radon transforms and show how this method can be used to decompose an image into dip-dependent data contribution. As we will show, this technique allows for the efficient separation of dips in the data by construction and also takes the local character of the data variations into account. We will start with the description of the theory and show subsequently in details how this algorithm was applied to extract the linear patterns in the GPR data set acquired at Turtle Mountain.

## 2. Theory

Our method for dip-dependent image decomposition is based on the assumption that the GPR data can be considered as a superposition of local wavefield operators. This idea is similar to the well known concept of Fourier synthesis, in which one constructs a signal from fundamental harmonics. However, instead of adding fundamental harmonic signals to synthesize the desired data, as it is the case for the Fourier synthesis, the data are constructed by a weighted sum of local 2-D functions or waveforms.

In our technique, multichannel data  $d(x, t)$  are represented as a superposition of temporal and spatially invariant operators as follows:

$$d(x, t) = \sum_{i=1}^N \sum_{x_0} \sum_{t_0} f(x_0, t_0, p_i) b(x - x_0, t - t_0, p_i). \quad (1)$$

$b(x, t, p)$  is a local wavefield operator in space-time parameterized by the ray parameter  $p$ . The second parameters,  $f(x_0, t_0, p_i)$ , are filter values that represent a measure of the data coherence in the neighborhood of a point  $(x_0, t_0)$  with respect to the dip  $p_i$ . Sacchi et al. (2004) interpreted these filters as shaping filters that transform the wavefield operators into the data.

Eq. (1) can also be written in matrix form as  $\mathbf{D} = \sum_i \mathbf{F}(p_i) \otimes \mathbf{B}(p_i)$  where the matrices  $\mathbf{D}$ ,  $\mathbf{F}(p_i)$  and  $\mathbf{B}(p_i)$  denote data, the Radon filters, and local wavefield operators, respectively. The convolution operator in Eq. (1) is now represented by the symbol  $\otimes$ .

The local wavefield operator is analytically written via the following expression:

$$b(x, t, p) = \mathcal{F}^{-1}[\tilde{b}(x, \omega, p)], \\ p = p_{\min}, \dots, p_{\max}. \quad (2)$$

The symbol  $\mathcal{F}^{-1}$  is used to indicate the inverse Fourier transform. The local wavefield operator in frequency-space is given by

$$\tilde{b}(x, \omega, p) = \tilde{s}(\omega) h(x) e^{i\omega p x}, \quad -\ell_0 \leq x \leq \ell_0. \quad (3)$$

In this expression,  $\tilde{s}(\omega)$  is the source signature or wavelet in the frequency domain. The variable  $h(x)$  is a spatial taper that gives larger weights to the center of the operator, the dip is denoted by  $p$ , and finally,  $\ell_0$  defines the operator half-aperture.

The local wavefield operators are parameterized with ray parameters or dips  $p_i$ ,  $i=1, \dots, N$ , where for simplicity we have adopted constant increment dips of the form  $p = p_{\min} + \Delta p(i-1)$ ,  $i=1, \dots, N$ , with minimum dip and increment chosen so as to span the dips present in the data. However, to avoid aliasing of the operators, the maximum dip must be chosen according to the criterion defined in Turner (1990):

$$p_{\max} = \frac{1}{2\Delta x f_{\max}} \quad (4)$$

where  $\Delta x$  is the spatial sampling distance.

Fig. 2 shows examples of three operators with different dips  $p$ . In this synthetic model, we have employed a Ricker wavelet with a center frequency of 50 MHz to approximate the source signal.

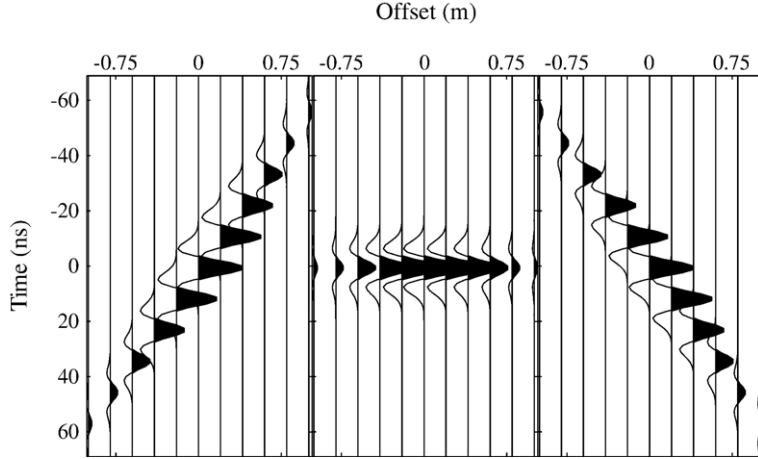


Fig. 2. Three wavefield operators. Left: minimum dip; center: zero dip; right: maximum dip. The 25 operators used in the analysis vary linearly between the minimum and maximum dip.

To avoid notational clutter we will concentrate on the compact expression  $\mathbf{D} = \sum_i \mathbf{F}(p_i) \otimes \mathbf{B}(p_i)$ . The Radon filters  $\mathbf{F}(p_i)$ ,  $i=1, \dots, N$  are obtained by solving a least squares problem. In this case, we find the operators  $\mathbf{F}(p_i)$  by minimizing the following cost function

$$J = \left\| \mathbf{D} - \sum_i \mathbf{F}(p_i) \otimes \mathbf{B}(p_i) \right\|^2 \quad (5)$$

The cost function  $J$  is a figure of data fidelity, in other words, we would like to find a set of Radon filters  $\hat{\mathbf{F}}(p_i)$ ,  $i=1, \dots, N$  that when convolved with local wavefield operators yield a signal that reproduces the original data within a predefined tolerance. At this point it is important to point out that the cost function  $J$  is minimized using the method of conjugate gradients (Sacchi et al., 2004). The advantage of using conjugate gradients is that computations can be done on the fly without the requirement of computing the inverse of large matrices. This strategy is very useful when computing large inverse problems such as those arising in Radon processing (Trad et al., 2003), and Migration/Inversion methods (Nemeth et al., 1999).

The set of Radon filters that minimize the cost function is designated as  $\hat{\mathbf{F}}(p_i)$ ,  $i=1, \dots, N$ . Once these operators are computed we are in condition of defining the following quantities:

- Data  $i$ th-mode,  $\hat{\mathbf{D}}_i = \hat{\mathbf{F}}(p_i) \otimes \mathbf{B}(p_i)$ , which models the data component with energy aligned in the  $p_i$  direction.
- By  $\hat{\mathbf{D}}_{\text{FR}} = \sum_{i=1}^N \hat{\mathbf{F}}(p_i) \otimes \mathbf{B}(p_i)$ , we denote the full reconstruction of the data using all the dips ( $p_i$ ),  $i=1, \dots, N$ . The associated error panel should contain random noise.

- $\hat{\mathbf{D}}_{\text{PR}} = \sum_{i \in I} \hat{\mathbf{F}}(p_i) \otimes \mathbf{B}(p_i)$  represents the partial reconstruction of the data using a subset of dips  $I$ , for instance, the dips containing modes that account for by most of the energy of the data.

The convolution operation employed when reconstructing the data and its similarity with the mathematical convolution operation (i.e., the product of two polynomials) leads to the term *generalized convolution* (Granlund and Knutsson, 1995). Similarly, we can consider the process of partially reconstructing the data as *generalized filtering*, and the technique of determining the filters  $\mathbf{F}(p_i)$  from the data as *generalized deconvolution*.

A few words about computational strategies to compute the Radon filters are in order. First, the number of iterations of the conjugate gradient method is used as a trade-off parameter (Hansen, 1998). In other words, the final iteration is reached when the data residuals do not contain visible coherent energy. In general this is achieved in 10–15 iterations. Secondly, the convolution and cross-correlation operations required by the method of conjugate gradients are performed using the Fast Fourier Transform (FFT) as described in Sacchi et al. (2004). The convolutional structure of Eq. (1) permits for fast operations in the frequency-wavenumber domain. The cost of each conjugate gradients iterations is proportional to the cost of 2D-FFTs times the number of dips ( $N$ ).

### 3. Field data example

We applied generalized deconvolution to a GPR data set that was acquired at the highly fractured summit of

Turtle Mountain in Alberta, Canada (see Theune et al., *in press*, for a detailed description of the surveys). The main purpose of these measurements was to detect fractures and to map bedding planes for geotechnical slope stability studies.

The data were acquired on steep slopes using a 50 MHz system. Numerous reflecting events in the subsurface complicated the analysis of the data substantially. Fig. 1 shows one of the acquired data sets after initial processing consisting of simple topographic corrections and amplitude gain. There are two dominating reflector patterns in the data that we have indicated by black and green arrows, respectively. In the following, we will refer to the fracture pattern indicated by black arrows as “downward dipping” events. The second pattern marked by green arrows will be referred to as “upward dipping” events. These reflections are most likely caused by bedding planes and fractures at the mountain’s summit.

The data were then migrated using a constant velocity Kirchhoff migration algorithm. The migration velocity that gave best results was found empirically to be  $v=0.08$  m/ns (Theune et al., *in press*). After migration, the image quality is even worse, as Fig. 3 shows. The detection of coherent events in the migrated image, which are related to bedding planes and fractures in the subsurface, is inhibited by the presence and superposition of numerous events with different dips. Nevertheless, the presence of two dominant linear reflector patterns may allow for successful dip-dependent image decomposition using the proposed technique.

### 3.1. Dip-dependent data decomposition

To facilitate the image analysis, in particular the determination of linear coherent features in the data,

we decomposed the data into 25 dip-dependent components, where the dip varied between  $-60.0$  and  $60.0$  ns/m. Since the wavelet of the propagating electro-magnetic wave is unknown, we approximated it by a Ricker wavelet with a central frequency of 50 MHz, which is the nominal frequency of the antennae system. Furthermore, we chose the aperture half-width ( $\ell_0$ ) to be 1 m, which is equivalent to including 11 GPR traces into the local operator. Finally, a Hamming window was used as the taper function  $h(x)$ . The size of the resulting local wavefield operator is  $111 \times 11$  sample, which is small compared to the size of the data set consisting of  $837 \times 465$  samples.

To evaluate the practicability and accuracy of the algorithm, we employed the following workflow for dip-dependent image decomposition (Fig. 4):

1. We start with the GPR data after initial processing consisting of topographic corrections, amplitude gain, and bandpass filtering.
2. Then, we migrate the data using a constant velocity Kirchhoff migration algorithm. The resulting image will be used as a benchmark for the data interpretation.
3. Using *generalized deconvolution*, we decompose the unmigrated data into  $N$  modes with different dips.
4. Now, we reconstruct the data using *generalized convolution*. This data set should be close to the original data.
5. Alternatively, we will use only a subset of the available data modes to extract certain dips in the data (i.e., *generalized filtering*). Then, we migrate the new data set to image and interpret the synthesized data. The interpretation of these data sets is then compared to the results of the original data to evaluate the usefulness of this algorithm.

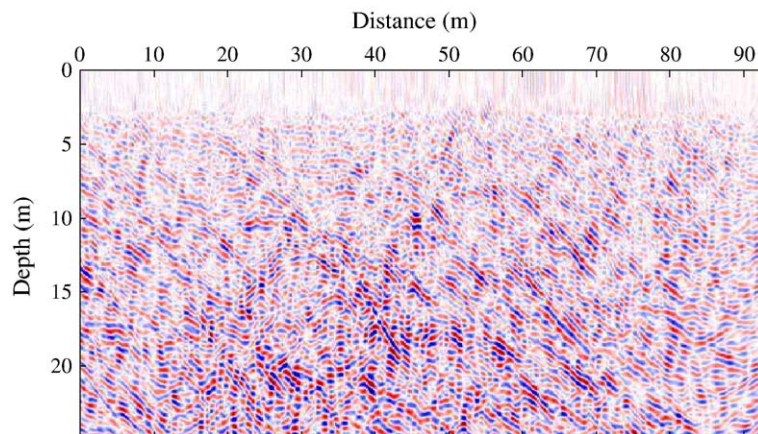


Fig. 3. The migrated GPR image using the original data. Note that the vertical axis is two-times exaggerated.

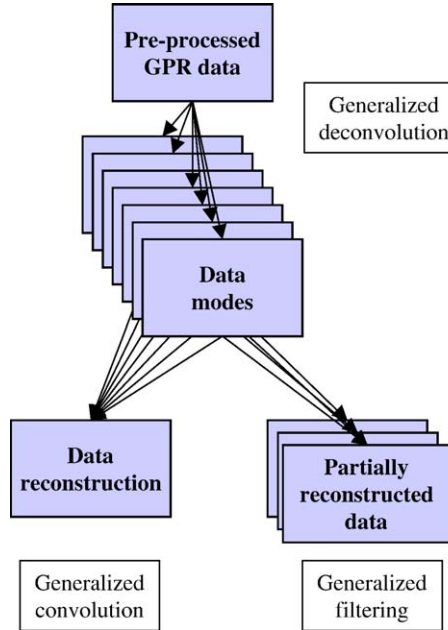


Fig. 4. Conceptual workflow for dip-dependent image decomposition.

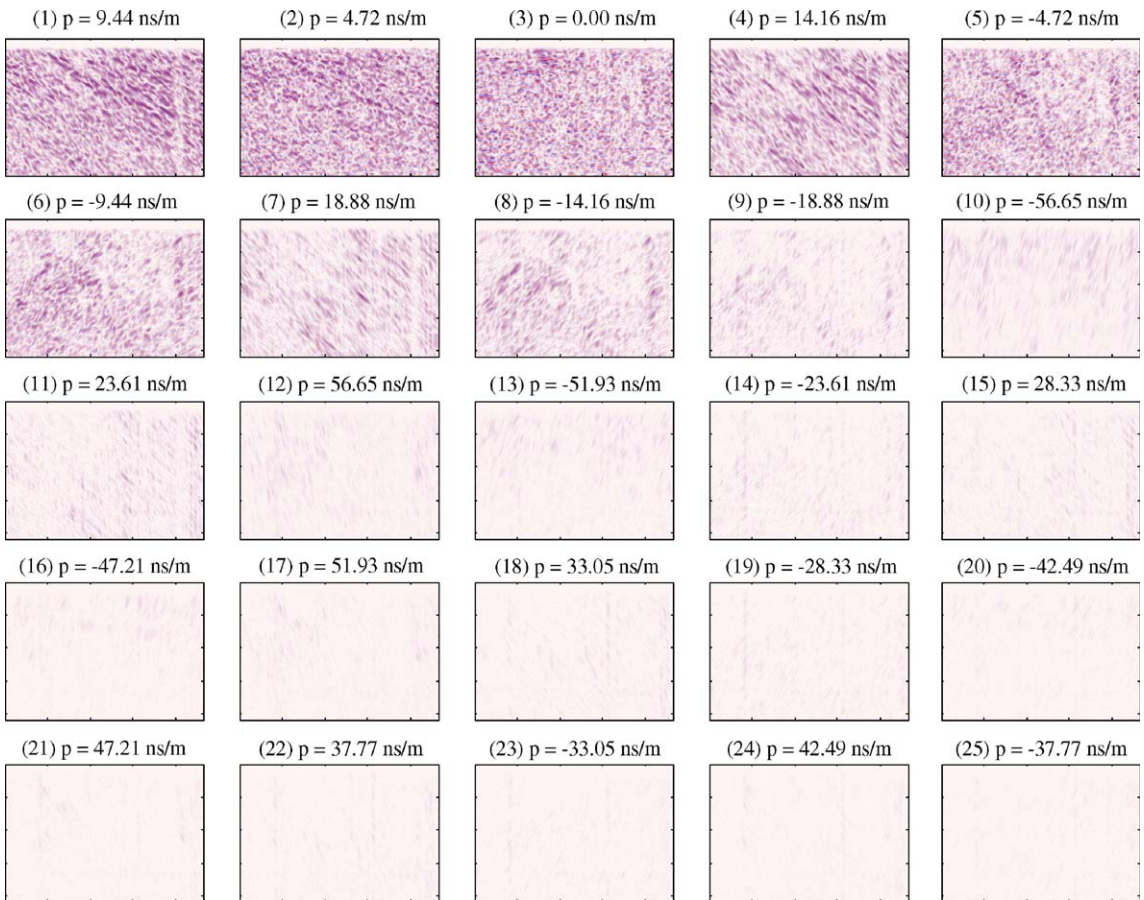


Fig. 5. The 25 dip-dependent data components of the original GPR data. The data are plotted versus offset and time as in Fig. 1; however, the axis labels have been omitted for the sake of clarity.

Fig. 5 displays the twenty-five data modes that we obtained after the application of the algorithm to the GPR data. The data modes are sorted such that the component with highest coherence energy appears in the top left corner (panel 1) and the one with least coherent energy is plotted in the bottom right corner (panel 25), where the coherence energy is calculated according to  $E_c(p) = \sum_{xt} d^2(x, t, p)$ . It is interesting to note that the first eight modes contain coherent data energy for dips that represent the “upward” and “downward dipping” events in the data. This shows that these two reflector patterns dominate the GPR image acquired at Turtle Mountain.

To test the decomposition algorithm, we first reconstruct the data set using all data components. The reconstruction is shown in Fig. 6 along with the original data and the difference between the reconstructed and original data set. The data difference plot shows that the reconstruction works well except for two regions. First, the algorithm is not able to model the abrupt change at

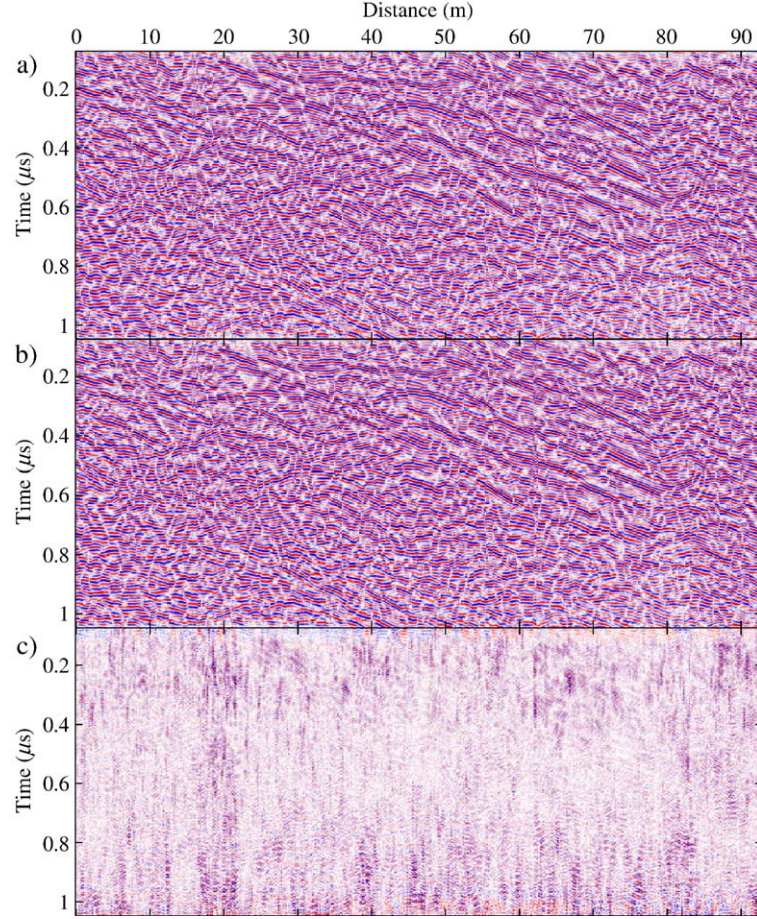


Fig. 6. Comparison of the original data (a) and the reconstructed data (b). c) Shows the reconstruction error amplified by a factor of 100.

short arrival times that has been introduced when truncating the direct wave in the data. This does, however, not pose a problem in our application as this sudden change is a processing artifact and can therefore be neglected. Secondly, the magnitude of the mismatches increases marginally for later arrival times. This effect may be explained by dispersion that distort the wave signal more for later arrival time, which is equivalent to longer travel paths of the wave. When designing the wavefield operators in Eq. (3), we assumed a constant wavelet. Therefore, the algorithm is prone to have difficulties in modelling the entire data set when the real wavelet is not constant. However, these discrepancies at later arrival times are small and can be neglected in this case.

Before continuing with the application of generalized filtering for data synthesis, we briefly demonstrate the significance of the filter panels  $f(x, t, p)$ . Fig. 7a shows the filter values calculated for a part of the data set where the upward dipping reflector apparently

dominates the data. However, there are more reflectors present with different dips in this part of the data set. This is also reflected in the wide range of the filter values. In fact, the analysis reveals that the strongest filter value is associated with a positive dip, i.e., a “downward” dipping reflection. This is contrasted by the data shown in Fig. 7b. Here, we have analyzed the data for a point where a continuous “downward” dipping event is present. The filter values show a narrow peak for the dip that represents the data locally best. Also, the maximum of the filter values is larger than for the first point. This shows that the filter values represent a measure for the local data coherence. We will return to this in the subsequent section.

We then applied generalized filtering to create two reconstructed data sets that contain only one of the dominating reflector pattern. From the 25 available data modes, we chose those that contain “downward” dipping energy. We will refer to this synthesized data set as  $D_{PR}^I$ . The second synthesized data set ( $D_{PR}^{II}$ )

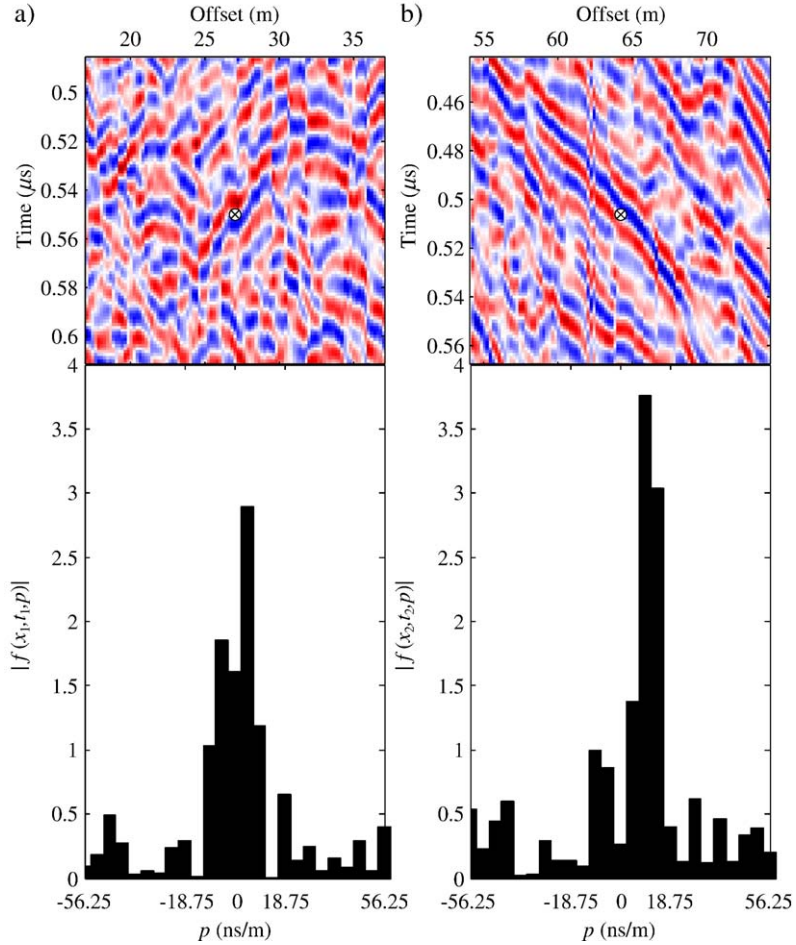


Fig. 7. The absolute values of the shaping filters are plotted for two points of the data sets (marked by  $\otimes$ ).

contains only upward dipping energy. The selected data modes are summarized in Table 1. We also include the coherence energy for the selected data mode normalized by the total data energy. These values underline the significance of the selected data modes in the data reconstruction process and in the synthesis of the data sets  $D_{\text{PR}}^{\text{I}}$  and  $D_{\text{PR}}^{\text{II}}$ , respectively. For instance, the data set  $D_{\text{PR}}^{\text{I}}$  accounts for 54.0% of the total data energy, the

second synthesized data set contributes 38.1% to the data energy, and the combined synthesized data sets contribute 92.1% to the data.

Subsequently, we applied constant velocity Kirchhoff migration (e.g. Yilmaz, 1987) to these data sets, the results of which are shown in Fig. 8. As before, we used a migration velocity of  $v=0.08$  m/ns. The section at the top results from migrating the original data. The interpretation of this image between 15 and 40 m profile length is complicated as numerous reflectors with different dips overlap in this part of the image. After dip-dependent decomposition, the interpretation of this part becomes much clearer. In addition, the decomposed data sets show much more coherent features after migration (middle and bottom panel). This becomes even more evident in the detail shown in Fig. 9. Coherent events, previously hidden behind superposing reflectors, appear clearly in the migrated data after image decomposition and the interpretation will be less ambiguous.

Table 1  
Data components used in the data synthesis

Data synthesis $D_{\text{PR}}^{\text{I}}$			Data synthesis $D_{\text{PR}}^{\text{II}}$		
Data mode	$p$ (ns/m)	$E_c/E_T \times 100\%$	Data mode	$p$ (ns/m)	$E_c/E_T \times 100\%$
1	9.44	19.6	3	0.00	14.6
2	24.72	18.7	5	-4.72	11.4
4	14.16	11.8	6	-9.44	8.2
7	18.88	3.9	8	-14.16	3.9
	$\sum = 54.0$			$\sum = 38.1$	

Refer to Fig. 5 for the meaning of the data mode numbers.

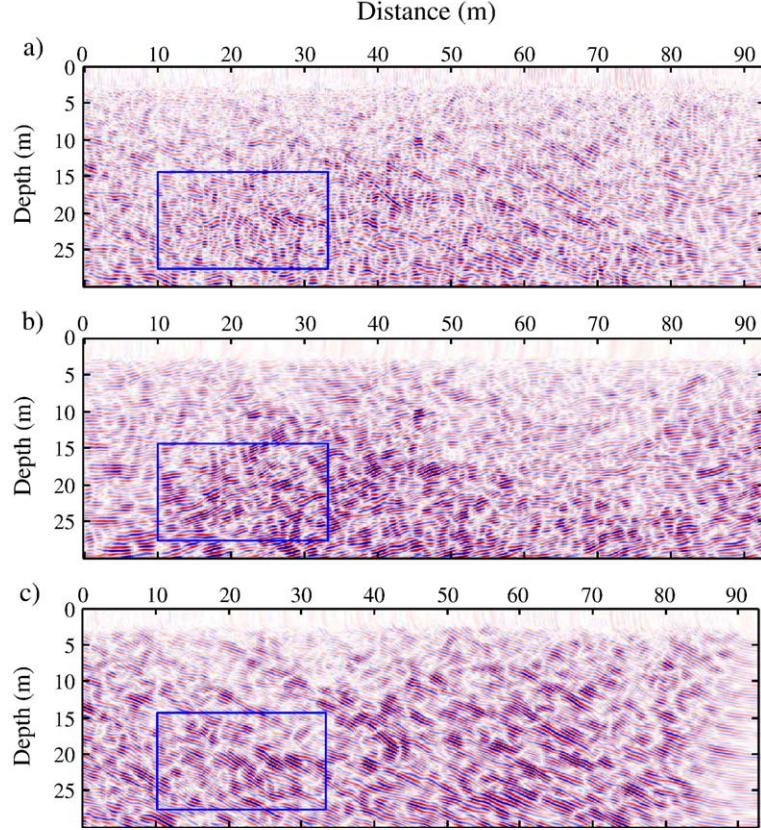


Fig. 8. Top: migration results using the original data. Center: image obtained using the synthesized data set  $D_{PR}^{II}$ . Bottom: migrated image using the synthesized data set  $D_{PR}$ . Fig. 9 shows the details enclosed in the blue box.

The improvement in image quality is also reflected in the interpretation of the data set shown in Fig. 10. This figure shows manually picked reflectors from the original data set (Fig. 10a) and a combination of the two synthetic data sets (Fig. 10b). The interpretation using the synthetic data sets shows not only much more details, but also the events seem to be more continuous compared to the interpretation of the original data.

### 3.2. Data coherence analysis

When deriving the local Radon operators, we interpreted the shaping filters  $f(x, t, p)$  as a measure of local data coherence. This interpretation of the values of the shaping filters at a point in the data set is also evident from the data shown in Fig. 7. When a point in a strongly coherent neighborhood is analyzed, the variation of  $f$ -values shows a narrow peak for the dominating dip (Fig. 7b). This is contrasted by a broad range of the  $f$ -values in Fig. 7a, when many data dips are present.

We now extend the analysis of the shaping filters. To investigate the potential of the shaping filters for data

coherence analysis, we create a map  $C(x, t)$  that for each point contains the maximum value of the filter values, i.e.,  $C(x, t) = \max_p [f(x, t, p)]$ . The values in the new data set represent a measure for the coherence of the neighborhood for a point  $(x, t)$ . Coherent events will appear as an alignment of large values in this data set, whereas areas of the data set with no coherent events will be represented by low values of  $C$ . A second attribute can be derived from the decomposition analysis, which is the dip value corresponding to the maximum filter value at each data point.

In Fig. 11, we compare the data set  $C$  with the GPR data. The top panel shows the original data, and the data set  $C$  is plotted in Fig. 11b. The third panel shows a map of the most coherent dip at each point of the data set. When comparing the images in Fig. 11a and b, the features present in the data are much clearer to see in the coherence attribute map  $C$ . The coherence value of features in the data that are smaller than the operator is much less than those for coherent events. Thus, small events in the data that we considered as “noise” are suppressed in the coherence map  $C$ . The second attri-

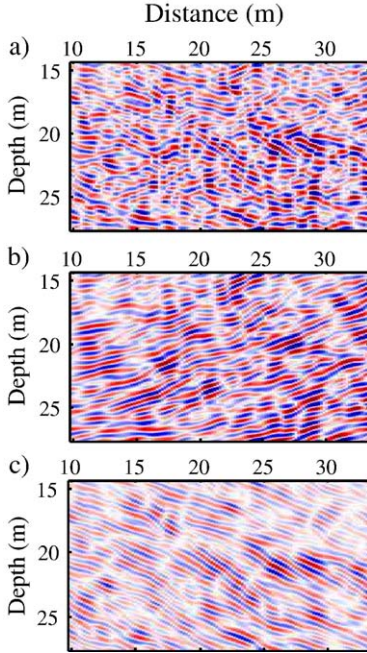


Fig. 9. Details of the migrated images in Fig. 8. Top: original data. Middle: “upward” dipping events. Bottom: “downward” dipping events.

bute map, displaying the data dip corresponding to the largest value of the filters, does unfortunately not show as many details. However, this map clearly indicates regions in the data where downward and upward dipping events dominate.

This approach to analyzing the coherent structure of data differs from the one by Marfurt et al. (1998) and others. The coherence technique commonly applied in seismic data analysis basically maps discontinuities of data coherence, which are related to geological structures, for example faults and river channels. However, these coherence analysis procedures do not work very well in the presence of significant amount of coherent noise, as it is the case for the GPR data from Turtle Mountain. On the other hand, utilizing the maximum value of the shaping filters leads to a representation of coherent events that resemble the geological structure very well.

#### 4. Discussion and conclusions

The concept of generalized convolution applied to local Radon transforms is a parametric processing algorithm that allows for the decomposition into and selective synthesis of local wavefield components. By choosing local linear Radon transforms for the wavefield operators, we were able to decompose a geophysical data set into dip-dependent components that reflect the local coherency structure of events in the data. Therefore, we can consider the resulting data components as the local coherency data modes of the data. The values of these data modes depend on the coherence of the data with respect to the dip and size of the decomposition operator. Local events in the vicinity of a data point with strong spatial and temporal coherency will

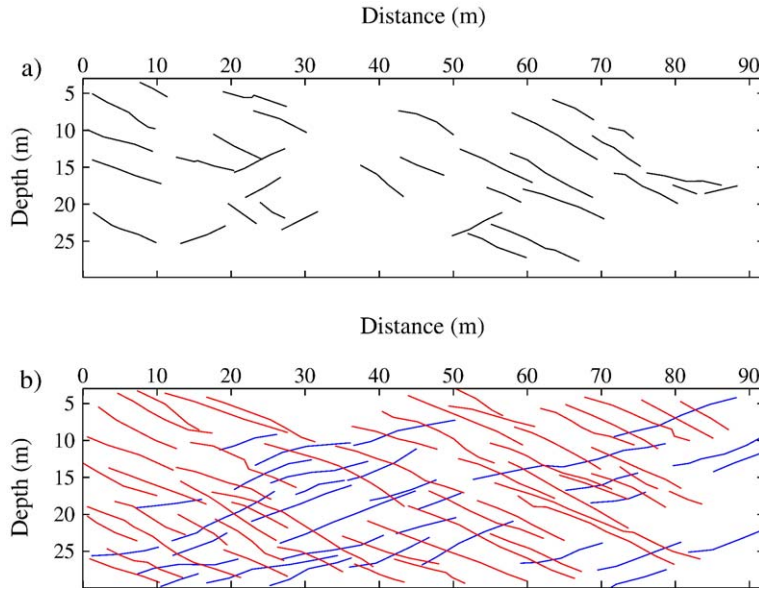


Fig. 10. Top: interpretation of the original data. Bottom: combined interpretation of the two synthesized images constructed using only “upward” and “downward” dipping data components (blue: “upward” dipping events, red: “downward” dipping events).

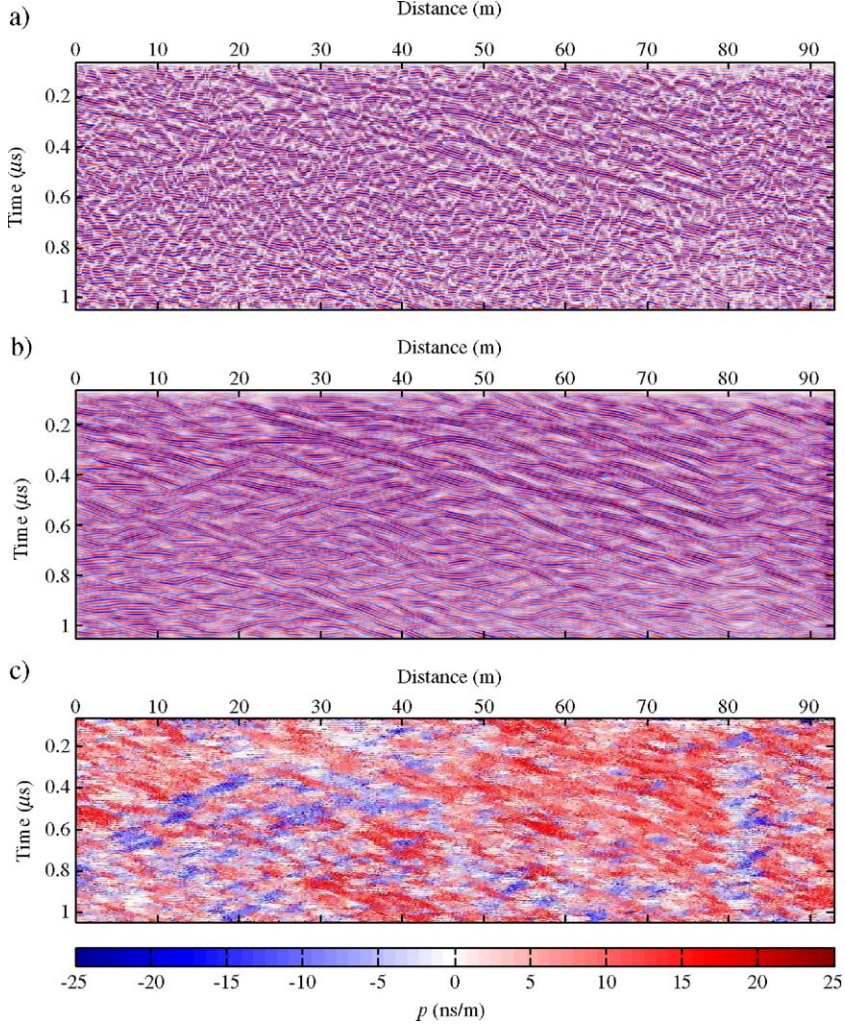


Fig. 11. a) Original data; b) maximum coherence attribute map, c) maximum dip attribute map.

result in a large value of the local coherence measure  $f(x, t, p)$ . These coherence measures then serve as operator weights in the image reconstruction process. By using only selected data modes, events with energetic and coherent dips can be extracted from the data for further analysis and migration.

The application of generalized deconvolution and filtering to the GPR data set demonstrate the potential of this algorithm. The synthetic data sets constructed by using only a small subset of the data modes improved the analysis and interpretation of the data substantially. After image decomposition and subsequent migration, linear coherent patterns in the data become much more apparent (Fig. 8). The detection of these events is significantly facilitated, which is also reflected in the interpretation of the data in Fig. 10. Whereas the interpretation of the original data shows discontinuous

reflectors, which are due to the difficulty in detecting coherent events, the combined interpretation of the two synthetic data sets shows considerably more details as well as continuity of the reflectors.

A few considerations on choosing the decomposition parameters follow. In our example, we have chosen a wide range for the dips  $p$ . As the data components in Fig. 5 show, modes with large dips do not contain much coherent energy. As such, we could have chosen a narrower dip range for the data decomposition. However, a proper range is difficult to estimate a priori, and therefore, choosing a wide range for  $p$  ensures that most, if not all, dips in the data are included in the decomposition. The second parameter to select is the half aperture width of the operator,  $\ell_0$ . If we choose a small value for  $\ell_0$ , short coherent features are recognized in the analysis. On the other hand, selecting a

larger operator mostly detects longer coherent features, whereas short events experience less weight in the generalized deconvolution process and are therefore suppressed in the image reconstruction. Hence, a proper choice for  $\ell_0$  depends on the data. In our example, we have chosen a value of 1 m for the aperture's half-width, which seems to be a good representative size of the average linear coherent reflectors in the migrated data (see Fig. 3). A proper choice for the center frequency of the modelled wavelet,  $\tilde{s}(\omega)$ , is difficult, especially in case of GPR data, as the propagating wavelet is often dispersive. In our example, we approximated the real wavelet by a synthetic Ricker wavelet with a center frequency of 50 MHz, which is the nominal frequency used in the data acquisition. The reconstruction test, shown in Fig. 6, indicates that this choice of  $\tilde{s}(\omega)$  is a proper one. The reconstruction error is generally small. Only for later arrival times, the mismatch of the original and reconstructed data increases. One reason for this can be that dispersive effects distort the real wavelet substantially such that the approximation by the synthetic wavelet is not as good as for earlier times. A second explanation can be that for later arrival times, data energy is reduced and random noise becomes dominating. In this case, the presence and detection of coherent events are reduced and the reconstruction of the data using generalized convolution does not recover the data anymore to a sufficient degree.

The filter values  $f(x, t, p)$  can serve as an attribute to analyze the coherence of the data. As shown in Fig. 11, this attribute map shows coherent events in the data much clearer than the actual GPR data. As this attribute is associated with the data coherence, it works well for data that are severely contaminated with noise. This is a major advantage over conventional coherence techniques (such as the one by Cohen and Coifman, 2002, among others), which display discontinuities of data coherence.

In conclusion, we have presented an algorithm that allows for dip-dependent image decomposition that takes the local coherence structure of the data set into account. This parametric technique was successfully employed to extract coherent features from a GPR data set that was severely contaminated with coherent noise. The algorithm is robust in such that the image reconstruction works well for low quality data as used in the example, even if an approximation to the wavelet  $\tilde{s}(\omega)$  must be used in constructing the operators.

Applications for this technique are numerous. Besides the extraction of coherent features in GPR data as

shown in this paper, this method can also be used to remove coherent and random noise, interpolation of missing traces, and wavefield separation.

## Acknowledgements

We like to thank David Cruden, Mike deGroot, Julia Holzhauer, Dan Kenway, Dean Rokosh, Marek Welz, and Willem Langenberg for their assistance in acquiring and interpreting the GPR data. The data acquisition and analysis were funded by NSERC, the Canada Research Chair program, both granted to D.R. Schmitt, and the SAIG consortium at the University of Alberta. The local Radon Matlab program is available at <http://www-geo.phys.ualberta.ca/saig/lwd>.

## References

- Cohen, I., Coifman, R.R., 2002. Local discontinuity measures for 3-D seismic data. *Geophysics* 67 (6), 1933–1945.
- Foster, M.R., Guinzy, N.J., 1967. The coefficient of coherence: its estimation and use in geophysical data processing. *Geophysics* 32 (4), 602–616.
- Goodman, D., Nishimura, Y., Rogers, J., 1995. GPR time slices in archaeological prospecting. *Archaeological Prospecting* 2, 85–89.
- Granolund, G.H., Knutsson, H., 1995. Signal Processing for Computer Vision. Kluwer Academic Publisher.
- Hampson, D., 1986. Inverse velocity stacking for multiple elimination. *Journal of the Canadian Society of Exploration Geophysicists* 22 (1), 44–55.
- Hansen, P.C., 1998. Rank-Deficient and Discrete Ill-Posed Problems: Numerical Aspects of Linear Inversion. SIAM.
- Mack, H., 1974. Coherence and structure. *Geophysics* 39 (1), 81–84.
- Marfurt, K.J., Kirlin, R.L., Farmer, S.L., Bahorich, M.S., 1998. 3-D seismic attributes using a semblance-based coherency algorithm. *Geophysics* 63 (4), 1150–1165.
- Nemeth, T., Wu, C., Schuster, G.T., 1999. Least-squares migration of incomplete reflection data. *Geophysics* 64, 208–221.
- Nuzzo, L., Quarta, T., 2004. Improvement in GPR coherent noise attenuation using  $\tau-p$  and wavelet transforms. *Geophysics* 69 (3), 789–802.
- Sacchi, M.D., Verschuur, D.J., Zwartjes, P.M., 2004. Data reconstruction by generalized deconvolution. In: SEG Society of Exploration Geophysicists (Ed.), 74th Annual International Meeting, Expanded Abstracts.
- Theune, U., Rokosh, C.D., Sacchi, M.D., Schmitt, D.R., in press. Mapping fractures with GPR: a case study from Turtle Mountain. Submitted for publication to *Geophysics*.
- Trad, D., Ulrych, T.J., Sacchi, M.D., 2003. Latest views of the sparse Radon transforms. *Geophysics* 68 (1), 386–399.
- Turner, G., 1990. Aliasing in the  $\tau-p$  transform and the removal of spatially aliased coherent noise. *Geophysics* 55 (11), 1496–1503.
- Yilmaz, Ö., 1987. Seismic data processing. vol. 2 of *Investigations in Geophysics*. Soc. of Expl. Geophys.
- Zeng, X., McMechan, G.A., 1997. GPR characterization of buried tanks and pipes. *Geophysics* 62, 797–806.